Original Article

Check for updates

Available online at
www.heca-analitika.com/hjas

Heca Journal of Applied Sciences

Vol. 4, No. 2, 2026

Electrical Resistivity Tomography for Mapping Landslide-Prone Zones in Pining Subdistrict, Gayo Lues, Aceh, Indonesia

Bukhari Ali [1,2], Nazli Ismail [2,*], Muhammad Syukri Surbakti [2], and Nasrullah Idris [2]

[1] Graduate School of Mathematics and Applied Sciences, Universitas Syiah Kuala, Banda Aceh 23111, Indonesia; bukhari.Ali.USK@gmail.com (B.A.)

[2] Department of Physics, Faculty of Mathematics and Natural Sciences, Universitas Syiah Kuala, Banda Aceh 23111, Indonesia; nazli.ismail@usk.ac.id (N.I.); msyukris@usk.ac.id (M.S.S.); nasrullah.idris@usk.ac.id (N.Id.)

***** Correspondence: nazli.ismail@usk.ac.id

Article History

Received 11 June 2026
Revised 3 July 2026
Accepted 8 July 2026
Available Online 25 August 2026

Keywords:
Subsurface heterogeneity
Conductive anomalies
Tropical weathering
Weak zones
Slope instability

Abstract

The interaction of topography, weathering, fracturing, lithological variability, and subsurface moisture controls slope instability in humid tropical terrain. This study maps resistivity heterogeneity and evaluates candidate weak zones on a slope showing evidence of movement in Pining Subdistrict, Gayo Lues Regency, using three intersecting electrical resistivity tomography (ERT) profiles. Data were acquired with a SuperSting R8/IP system using a Wenner-Schlumberger array, 55 electrodes at 6 m spacing, and a 324 m profile length. The apparent-resistivity data were inverted in EarthImager 2D using an L2-norm smooth-model scheme with electrode elevations incorporated into the inversion mesh. Inversion terminated after four iterations for Profiles 1 and 2 and five iterations for Profile 3, with final RMS misfits of 11.62%, 11.41%, and 10.42%, respectively. The inverted resistivity models delineate a near-surface high-resistivity domain (>1000 Ohm.m) overlying intermediate- and low-resistivity domains. Broad spatial correspondence is observed between conductive anomalies S1 and S6, S2 and S7, and S3 and S8 on Profiles 1 and 3, whereas conductive anomaly S5 on Profile 2 is spatially associated with S1 and S6 near the profile intersections. Conductive anomalies S1, S5, and S6 have the strongest cross-profile support. Considering the resistivity distribution, geological setting, field evidence of slope movement, and monthly rainfall context, the principal conductive anomalies are interpreted as intensely weathered, locally fractured, and comparatively moist material. The resistivity-gradient boundary at approximately 10-50 m depth marks a geoelectrical transition and is treated as a candidate weak-zone boundary rather than a confirmed slip surface; hydrogeological and geotechnical validation is required.

1. Introduction

Landslides are downslope movements of soil, debris, or rock that occur when driving stresses exceed the shear resistance of slope materials. Such events can disrupt transportation networks, settlements, and productive land; therefore, risk reduction requires an understanding of both triggering processes and the internal condition of the slope [1]. In humid tropical environments, intense chemical weathering produces thick regolith with strongly variable strength, porosity, and permeability. Prolonged or intense rainfall may enhance infiltration and pore-water pressure, reduce effective stress or matric suction, and accelerate deformation within pre-weakened slope materials [2].

Surface morphology alone does not necessarily reveal the subsurface structures that govern slope instability. A single slope may contain contacts between relatively competent and intensely weathered materials, clay-rich horizons, fracture-controlled flow paths, and zones of subsurface water accumulation. These heterogeneities influence preferential flow and strain localization but are not always identifiable from surface observations. Subsurface characterization is therefore required to evaluate whether visible slope movement is associated with contrasts in material properties at depth [3].

Geophysical methods provide spatially continuous information between direct observation points and can complement geomorphological mapping and geotechnical investigation. Electrical resistivity tomography (ERT) is widely applied to landslide studies because bulk electrical resistivity is sensitive to water content, porosity, pore-fluid salinity, clay content, weathering intensity, and fracturing [4]. Time-lapse ERT can detect resistivity changes associated with infiltration and the development of critically saturated conditions [5, 6]. Integration of ERT with hydrological observations can further constrain moisture dynamics on slopes susceptible to shallow failure [7].

The relationship between electrical resistivity and mechanical condition is inherently non-unique. Low resistivity may reflect high water content, conductive clay minerals, intense weathering, fluid-filled fractures, or a combination of these factors [3]. Conversely, relatively dry weathered material may retain high resistivity [4]. A resistivity contrast therefore cannot be interpreted as a slip surface without geological, hydrogeological, or geotechnical support [8]. Interpretation is more robust when geoelectrical anomalies are evaluated against seismic or geotechnical data [9, 10], while multi-profile or three-dimensional surveys help assess anomaly persistence and possible off-profile effects [11].

Geophysical investigations of landslides in Aceh have been conducted in several geological settings. Integrated ERT, induced polarization, and VLF-EM surveys at Lamreh differentiated variations in stratification, fracturing, and water content along a coastal cliff [12]. In the Blangkejeren-Gayo Lues area, ERT was used to image resistivity contrasts among subsurface materials [13]. In contrast, seismic refraction tomography provided complementary information on P-wave velocity variations within weathered slope materials [14]. Unlike the Lamreh investigation, which integrated several geophysical methods in a coastal-cliff setting, the present study uses three intersecting ERT profiles to evaluate the spatial consistency of conductive anomalies on a humid tropical mountain slope.

The Pining site was selected because exposed and displaced slope material and disruption of a local access track provide field evidence of slope movement. A verified historical inventory for the investigated slope is unavailable; accordingly, the term landslide-prone zones in this study refers to candidate geoelectrical weak zones inferred from the combined field observations and resistivity patterns, rather than to a regional landslide-susceptibility class. This study aims to characterize the two-dimensional resistivity distribution along three intersecting profiles, compare anomaly positions, depths, and resistivity ranges across profiles, and identify candidate weak-zone boundaries associated with slope instability. The methodological contribution is the use of cross-profile spatial correspondence to distinguish recurrent geoelectrical patterns from isolated features and possible three-dimensional effects.

2. Materials and Methods

2.1. Geological Setting of the Study Area

The study area is located in Pining Subdistrict, Gayo Lues Regency, Aceh, within approximately 97°24′25.3″-97°24′36.0″ E and 4°03′03.0″-4°03′15.0″ N. Endpoint coordinates were recorded with a handheld GPS and are reported as approximate field positions. Gayo Lues is dominated by mountainous terrain; approximately 43.93% of the regency has slope angles greater than about 21.8° [15]. Most of the regency lies at elevations of 1000-2000 m above sea level [15]. Elevations along the ERT profiles range from approximately 1563 to 1614 m, indicating a highland slope with irregular local relief.

Regionally, the site lies near the contact between the sedimentary Rampong Formation and the predominantly metamorphic Kluet Formation; the Peutu Formation and alluvial deposits also occur in the surrounding area (Figure 1) [16]. The Sumatran Fault System defines the regional structural framework and may be associated with fracture development and differential weathering [17]. Fault segmentation and lithological contacts can also generate permeability contrasts that influence subsurface moisture distribution and the measured resistivity response [18].

Field observations documented exposed intensely weathered material, displaced ground surfaces, and disruption of a local access track. Satellite imagery shows that the disturbed area forms an unvegetated surface adjacent to a winding road on the slope (Figure 2). These observations were used to select the survey area but were not treated as direct evidence of the depth or geometry of a subsurface slip surface.

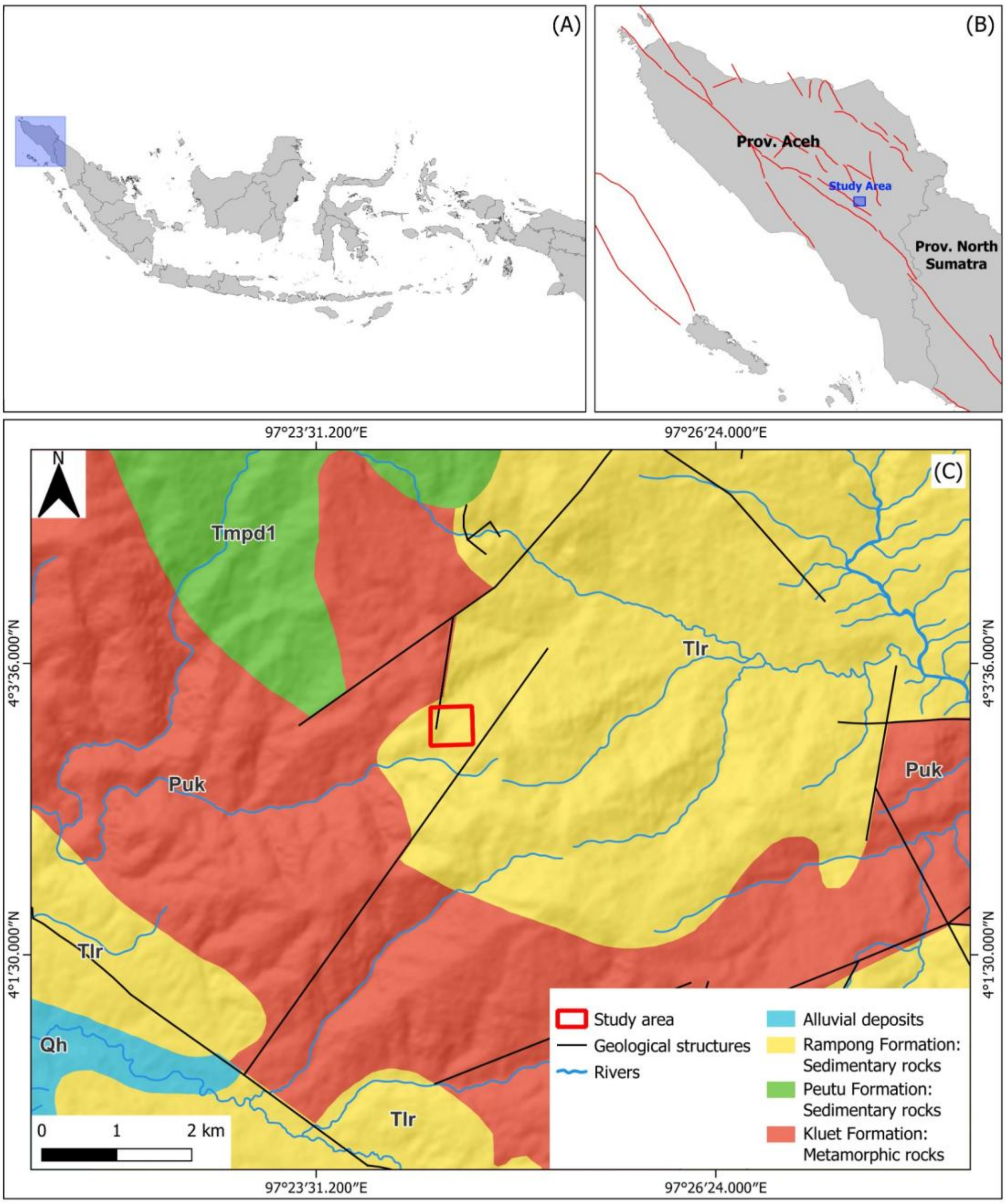

Figure 1. Location and regional geological setting of the study area: (A) location of Aceh within Indonesia, (B) position of the study area relative to the regional fault system, and (C) geological formations surrounding Pining. The geological map was modified from Cameron et al. [16].

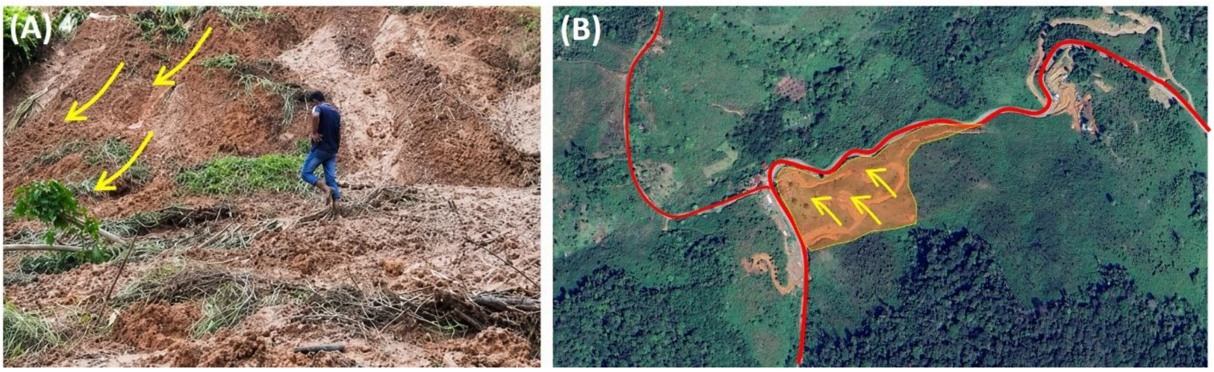

Figure 2. Evidence of slope instability at the study site: (A) intensely weathered material and a displaced ground surface; (B) location of the disturbed area on satellite imagery. Arrows indicate the general direction of material movement.

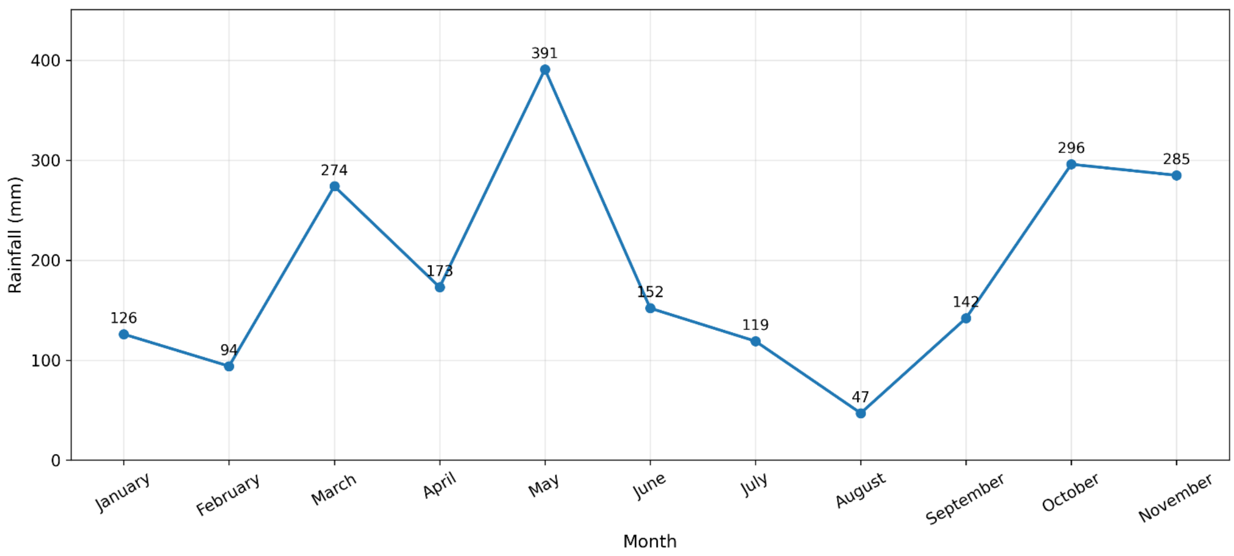

Figure 3. Monthly rainfall at the Pining observation station from January to November 2019, based on data from BPS-Statistics of Gayo Lues Regency [15]. ERT acquisition was conducted in June 2019.

2.2. Data Acquisition and Inversion

ERT data were acquired in June 2019. The Pining observation station recorded monthly rainfall totals of 391 mm in May and 152 mm in June 2019 [15]. These totals provide monthly hydroclimatic context and are not used to infer antecedent water content or the degree of subsurface saturation during acquisition. Figure 3 shows monthly rainfall from January to November 2019; December data were unavailable in the source used.

Three ERT profiles were designed to sample resistivity variations along different orientations. Profile 1 trends approximately E-W, Profile 3 trends SW-NE, and Profile 2 trends S-N and intersects both profiles in the western survey sector (Figure 4). This oblique geometry permits comparison of anomaly positions between the two broadly east-trending profiles and cross-checking along a transverse profile. Because the ground surface is irregular, we did not assign a single mean slope angle to each profile; instead, we measured the elevation of every electrode and incorporated it directly into the inversion mesh.

Measurements were acquired with a SuperSting R8/IP system using a Wenner-Schlumberger array. Each profile comprised 55 electrodes at 6 m spacing, giving a length of 324 m from the first to the last electrode. The Wenner-Schlumberger array was selected because it provides sensitivity to both lateral and vertical resistivity variations while maintaining adequate signal strength in irregular terrain [19]. Apparent resistivity was calculated from the injected current and measured potential difference using Equation (1):

$$\rho_a = K\frac{\Delta V}{I} \qquad (1)$$

where ρ_a is apparent resistivity, K is the geometric factor of the electrode configuration, ΔV is the measured potential difference, and I is the injected current.

The apparent-resistivity data were visually inspected in EarthImager 2D before inversion, and the complete dataset was retained. The data were inverted using an L2-norm smooth-model scheme, with the mesh surface constrained by electrode elevations measured using a handheld GPS. The starting model was generated from the apparent resistivity pseudosection, with resistivity bounds of 1-10000 Ohm.m. Table 1 summarizes the inversion settings, regularization parameters, stopping criteria, and final RMS misfits. RMS misfit quantifies the discrepancy between measured and calculated apparent resistivities and was not used as the sole criterion for geological reliability.

The displayed inverted resistivity models extend to approximately 50-60 m below the ground surface, but this range was not treated as a uniform depth of reliable investigation. Model sensitivity and depth-of-investigation (DOI) outputs were unavailable; therefore, anomalies approaching the lower model boundary, particularly S1, S2, S4, and S5, were interpreted with reduced confidence [20].

3. Results and Discussion

Interpretation emphasized relative resistivity contrasts within each section because the color scales and minimum inverted resistivity values differ among profiles. For this dataset, values generally >1000 Ohm.m were treated as a near-surface high-resistivity domain, values of approximately 100-1000 Ohm.m as an

Table 1. ERT acquisition and inversion parameters.

Parameter	Specification
Acquisition month	Jun-19
Instrument and array	SuperSting R8/IP; Wenner-Schlumberger
Electrodes, spacing, and length	55 electrodes; 6 m spacing; actual profile length 324 m
Profile 1	Approximately E-W; start 97°24′25.3″ E, 4°03′11.4″ N; end 97°24′36.0″ E, 4°03′11.0″ N
Profile 2	Approximately S-N; start 97°24′27.7″ E, 4°03′03.0″ N; end 97°24′26.2″ E, 4°03′13.1″ N
Profile 3	Approximately SW-NE; start 97°24′25.3″ E, 4°03′11.6″ N; end 97°24′34.6″ E, 4°03′15.0″ N
Surface elevation	Profile 1: ~1591-1614 m; Profile 2: ~1586-1607 m; Profile 3: ~1563-1594 m
Topographic input	Electrode elevations measured using a handheld GPS and incorporated into the 2D inversion mesh
Data inspection	Visual inspection of apparent-resistivity data; complete dataset retained; separate contact-resistance records were unavailable for additional filtering
Inversion scheme	EarthImager 2D; L2-norm smooth-model inversion
Starting model and resistivity bounds	Starting model generated from the pseudosection; bounds of 1-10000 Ohm.m
Regularization	Smoothness factor 10; damping factor 10; horizontal/vertical roughness ratio 0.5
Numerical parameters	Estimated data noise 3%; 6 conjugate-gradient iterations; resolution factor 0.2
Stopping criteria	Maximum 8 iterations; target RMS 3%; minimum error reduction 5%
Final iterations and RMS misfit	Profile 1: 4 iterations, 11.62%; Profile 2: 4 iterations, 11.41%; Profile 3: 5 iterations, 10.42%
Reliability constraint	Model sensitivity and DOI outputs unavailable; features approaching the lower model boundary interpreted cautiously

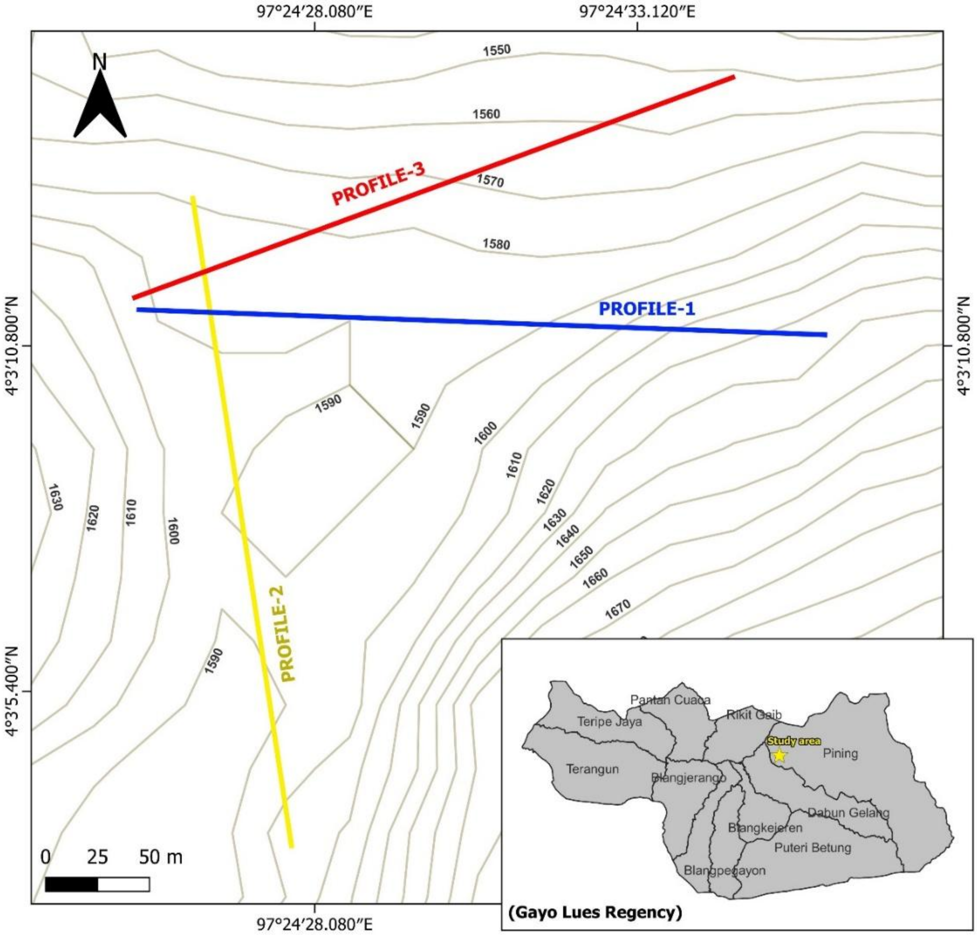

Figure 4. Configuration of the three ERT profiles superimposed on topographic contours. Profile 1 trends approximately E-W, Profile 3 trends SW-NE, and Profile 2 trends S-N and intersects both profiles in the western sector.

intermediate-resistivity domain, and values <100 Ohm.m as the most conductive parts of the models. The labelled anomalies are relatively low-resistivity bodies compared with their immediate surroundings and may include both low- and intermediate-resistivity values. These thresholds are operational descriptors for this dataset rather than universal lithological classes. The dashed line generally follows the strongest laterally persistent

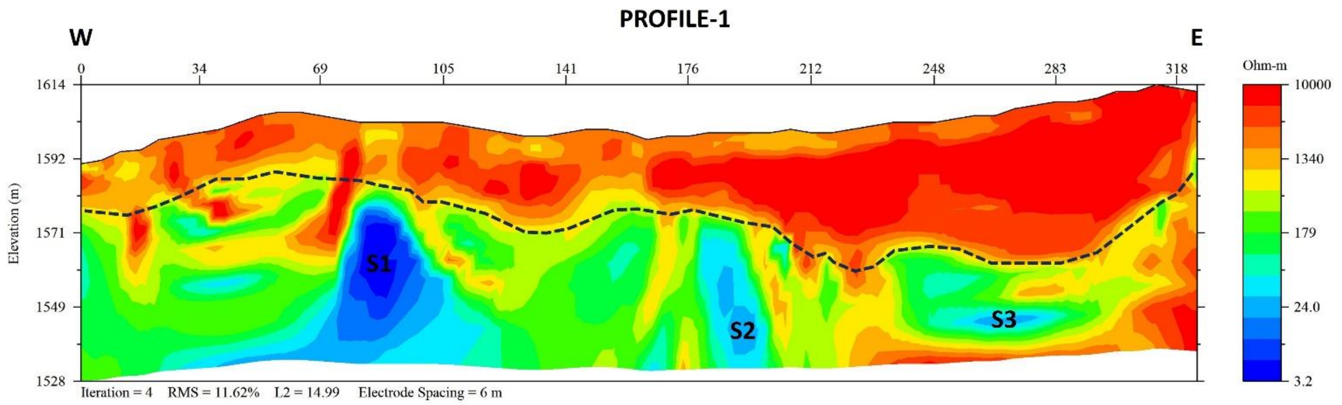

Figure 5. Two-dimensional resistivity model of Profile 1. S1-S3 denote conductive anomalies; the dashed line follows the resistivity gradient interpreted as a candidate weak-zone boundary.

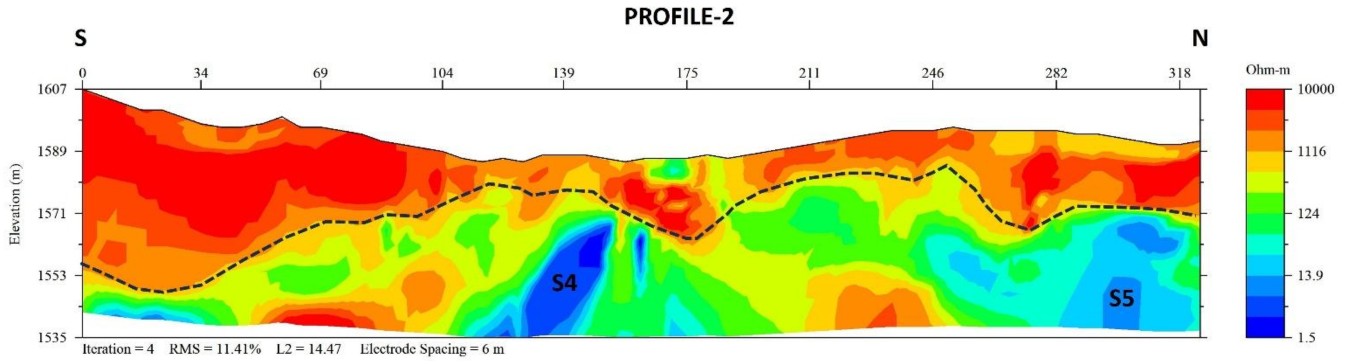

Figure 6. Two-dimensional resistivity model of Profile 2, oriented south-north. S4 and S5 denote conductive anomalies; the dashed line marks the candidate weak-zone boundary.

gradient near the transition from the >1000 Ohm.m domain to underlying lower-resistivity material; it is not a fixed 1000 Ohm.m isoresistivity contour. This boundary is termed a candidate weak-zone boundary and is not regarded as a confirmed slip surface.

Profile 1 trends approximately E-W, with surface elevations of approximately 1591-1614 m and inverted resistivity values of 3.2-10000 Ohm.m. A near-surface high-resistivity domain is extensive, particularly from about 170 m to the eastern end of the profile. Three conductive anomalies occur beneath this domain. Conductive anomaly S1 lies between approximately 80 and 110 m, has dominant resistivities of 3.2-24 Ohm.m, begins at about 20 m depth, and extends beyond 50 m depth. Conductive anomaly S2 occurs between about 175 and 210 m, with resistivities mainly <179 Ohm.m at depths of approximately 25-55 m. Conductive anomaly S3 forms an elongate relatively low-resistivity body between approximately 250 and 285 m at depths of about 25-50 m (Figure 5).

The principal resistivity-gradient boundary on Profile 1 occurs at approximately 10-40 m depth and locally deepens between 200 and 280 m. S1 and S2 have pronounced subvertical geometries and extend toward the lower model boundary; therefore, their maximum depths cannot be resolved reliably. S3 is more laterally extensive and occurs beneath the high-resistivity surface domain. These geometries indicate strong lateral and vertical heterogeneity but do not independently identify lithology or mechanical discontinuities.

Profile 2 trends south-north and intersects the other profiles in the western survey sector. Surface elevations range from approximately 1586 to 1607 m, and inverted resistivity values span 1.5-10000 Ohm.m. A near-surface high-resistivity domain dominates the southern sector, whereas the central and northern sectors are more heterogeneous. Conductive anomaly S4 occurs between approximately 130 and 165 m, with dominant resistivities of 1.5-13.9 Ohm.m; it begins at about 20 m depth and extends to the lower model boundary. Conductive anomaly S5 occurs between 270 and 318 m in the northern sector, with resistivities of 13.9-124 Ohm.m at depths of approximately 20-50 m. The principal resistivity-gradient boundary lies at approximately 10-50 m depth and deepens around S5 (Figure 6).

S4 has the lowest resistivity on Profile 2, but it is detected on only one section and extends to the lower model boundary. In contrast, S5 occurs near the profile

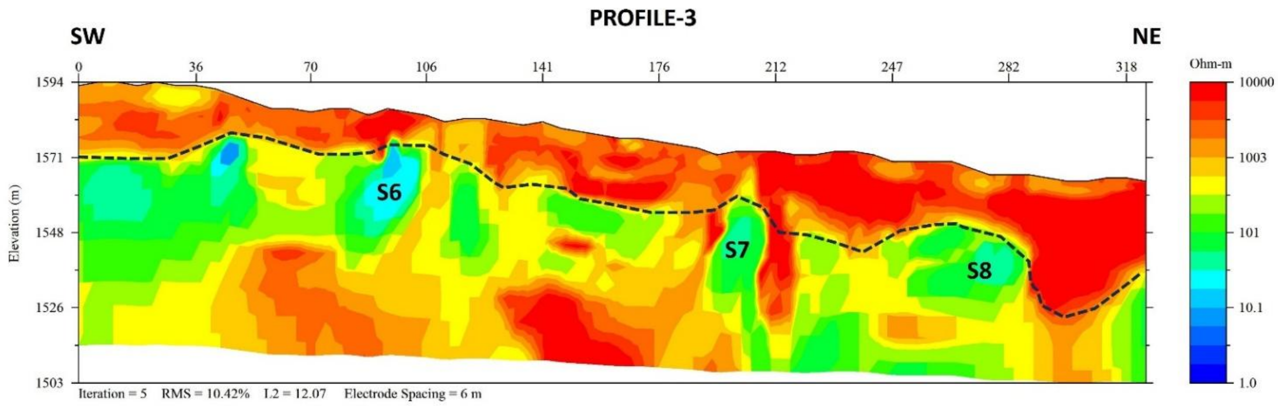

Figure 7. Two-dimensional resistivity model of Profile 3. S6-S8 denote conductive anomalies; the dashed line marks the candidate weak-zone boundary.

Table 2. Cross-profile synthesis of conductive anomalies.

Group	Profile 1	Profile 2	Profile 3	Interpretive synthesis
A	S1; 80-110 m; 3.2-24 Ohm.m; depth ~20 to >50 m	S5; 270-318 m; 13.9-124 Ohm.m; depth ~20-50 m	S6; 80-110 m; 10.1-101 Ohm.m; depth ~10-35 m	Strongest cross-profile correspondence, detected on all three profiles and across profiles with different orientations; highest priority for hydrogeological and geotechnical validation.
B	S2; 175-210 m; <179 Ohm.m; depth ~25-55 m	-	S7; 195-215 m; 10.1-101 Ohm.m; depth ~15-45 m	Paired conductive anomalies on the two obliquely oriented east-trending profiles; continuity remains unverified.
C	S3; 250-285 m; <179 Ohm.m; depth ~25-50 m	-	S8; 250-285 m; 10.1-101 Ohm.m; depth ~20-40 m	Recurrent conductive anomalies in the eastern sector; continuity remains unverified.
D	-	S4; 130-165 m; 1.5-13.9 Ohm.m; depth ~20 to >50 m	-	Highly conductive but isolated anomaly extending to the lower model boundary; possible localized heterogeneity or off-profile structure.

intersections and has a position and depth range comparable to S1 and S6. Cross-profile support for S5 is therefore stronger than for S4, despite S4's lower minimum resistivity.

Profile 3 trends SW-NE, with surface elevations of approximately 1563-1594 m and inverted resistivity values of 1.0-10000 Ohm.m. The near-surface high-resistivity domain is discontinuous and overlies three conductive anomalies. Conductive anomaly S6 occurs between 80 and 110 m, with dominant resistivities of 10.1-101 Ohm.m at depths of approximately 10-35 m. Conductive anomaly S7 occurs between 195 and 215 m. It extends from approximately 15 to 45 m depth, whereas conductive anomaly S8 lies between 250 and 285 m and forms a relatively low-resistivity body at approximately 20-40 m depth. The principal resistivity-gradient boundary generally lies at 10-40 m depth and deepens in the eastern sector (Figure 7).

Cross-profile comparison indicates broad spatial correspondence between conductive anomalies S1 and S6, S2 and S7, and S3 and S8. The comparison is based on their relative positions, geometries, and depth ranges along Profiles 1 and 3. Because these profiles are oblique and diverge eastward, the relationships are interpreted as recurring geoelectrical patterns rather than direct evidence of continuous three-dimensional bodies. Near the profile intersections, conductive anomaly S5 on Profile 2 is spatially associated with S1 and S6. The inferred relationships therefore remain hypotheses that require three-dimensional imaging or direct subsurface validation.

For synthesis, the conductive anomalies were grouped only according to cross-profile correspondence (Table 2). Group A comprises S1, S5, and S6 and has the strongest support because its components are detected on all three profiles and across profiles with different orientations. Groups B and C comprise the paired anomalies S2 and S7 and S3 and S8, respectively. Group D consists only of S4 and therefore represents an isolated anomaly. This grouping is an interpretive ranking framework, not a geological or geotechnical classification; it demonstrates that minimum resistivity alone is insufficient for prioritization and that spatial consistency and survey geometry provide additional constraints.

A near-surface high-resistivity domain overlying lower-resistivity material has also been reported in ERT investigations of landslides in Hunan, China [21], Ali Mendjeli, Algeria [22], and along the Cisumdawu Highway in West Java [23]. However, interpretation of a resistivity contrast as a slip surface is more robust when supported by independent seismic or geotechnical constraints, as demonstrated at Vallcebre [9] and on a residual-soil slope [10]. Such direct constraints are unavailable at Pining; therefore, similarity in resistivity architecture is used to identify candidate weak zones rather than to assign lithology or definitively delineate a slip surface.

The principal conductive anomalies are most plausibly associated with intensely weathered material containing localized fractures and greater moisture content than the overlying high-resistivity domain. This interpretation is consistent with field evidence of slope movement, the regional geological setting, and the monthly rainfall context. Rainfall-related slope response depends on antecedent hydrological conditions and site-specific drainage regimes [24, 25]. Increased moisture can reduce bulk resistivity and, within pre-weakened material, may reduce matric suction or increase pore-water pressure [5, 6]. Clay enrichment and lithological variation can nevertheless produce comparable low-resistivity responses; therefore, moisture-related weakening is presented as a testable hypothesis rather than a demonstrated failure mechanism.

The recurrence of anomalies in two survey orientations provides stronger constraints than interpretation from a single profile. Three-dimensional investigations of active landslides have shown that drainage pathways and anomaly geometry may vary outside a two-dimensional section [11]. At Pining, features that recur across profiles are prioritized for further investigation, whereas S4 is treated cautiously because it may represent localized heterogeneity or an off-profile structure.

The absence of borehole data, groundwater-level measurements, shear-strength tests, and displacement monitoring limits the interpretation. The monthly rainfall series does not resolve short-term antecedent moisture conditions. The absence of model sensitivity and DOI analyses increases uncertainty in the deepest parts of the inverted resistivity models [20]. In addition, two-dimensional inversion assumes negligible resistivity variation perpendicular to the profile; where this assumption is violated, off-profile structures may distort anomaly geometry [8]. The different profile orientations reduce interpretive ambiguity through cross-profile comparison but do not replace three-dimensional imaging.

The combination of oblique and intersecting profiles helps distinguish recurring geoelectrical patterns from isolated features without removing the inherent non-uniqueness of resistivity interpretation. The study objectives were met by characterizing the resistivity distribution, identifying conductive anomalies, and evaluating their broad spatial correspondence across profiles. Conductive anomalies S1, S5, and S6 are the highest-priority targets for borehole verification, groundwater monitoring, geotechnical testing, and deformation monitoring, whereas S4 requires additional evidence before it can be associated with slope instability.

4. Conclusions

Three intersecting ERT profiles reveal a heterogeneous subsurface beneath the Pining slope, characterized by a near-surface high-resistivity domain (>1000 Ohm.m) overlying intermediate- and low-resistivity domains. Broad spatial correspondence is observed between conductive anomalies S1 and S6, S2 and S7, and S3 and S8 on Profiles 1 and 3, while conductive anomaly S5 on Profile 2 is spatially associated with S1 and S6 near the profile intersections. Conductive anomalies S1, S5, and S6 provide the strongest cross-profile evidence for a candidate weak zone, whereas S4 remains less certain because it is isolated and extends to the lower model boundary. The resistivity-gradient boundary at approximately 10-50 m depth marks a geoelectrical transition from the near-surface high-resistivity domain to lower-resistivity material, interpreted as more intensely weathered, locally fractured, and comparatively moist. The data do not demonstrate a mechanically defined slip surface or a groundwater-controlled failure mechanism. The study's principal contribution is using anomaly consistency across profiles with different orientations to prioritize candidate weak zones. Further validation should combine boreholes, groundwater monitoring, geotechnical testing, deformation measurements, model sensitivity analysis, DOI analysis, and three-dimensional resistivity imaging.

Author Contributions: Conceptualization, B.A. and N.I.; methodology, B.A., M.S.S., and N.I.; software, B.A. and M.S.S.; validation, N.I., M.S.S., and N.Id.; formal analysis, B.A.; investigation, B.A.; resources, N.I. and N.Id.; data curation, B.A. and M.S.S.; writing-original draft preparation, B.A.; writing-review and editing, N.I., M.S.S., and N.Id.; visualization, B.A.; supervision, N.I., M.S.S., and N.Id.; project administration, N.I. All authors have read and agreed to the published version of the manuscript.

Funding: This study does not receive external funding.

Ethical Clearance: Not applicable.

Informed Consent Statement: Not applicable.

Data Availability Statement: Data supporting the findings of this study are available from the corresponding author upon reasonable request.

Acknowledgments: The authors thank the field team and local stakeholders in Pining Subdistrict, Gayo Lues Regency, for their support during field data collection.

Conflicts of Interest: All the authors declare no conflicts of interest.

References

1. Capobianco, V., Choi, C. E., Crosta, G., Hutchinson, D. J., Jaboyedoff, M., Lacasse, S., Nadim, F., and Reeves, H. (2025). Effective Landslide Risk Management in Era of Climate Change, Demographic Change, and Evolving Societal Priorities, *Landslides*, Vol. 22, No. 9, 2915–2933. doi:10.1007/s10346-024-02418-2.
2. Amarasinghe, M. P., Kulathilaka, S. A. S., Robert, D. J., Zhou, A., and Jayathissa, H. A. G. (2024). Risk Assessment and Management of Rainfall-Induced Landslides in Tropical Regions: A Review, *Natural Hazards*, Vol. 120, No. 3, 2179–2231. doi:10.1007/s11069-023-06277-3.
3. Whiteley, J. S., Chambers, J. E., Uhlemann, S., Wilkinson, P. B., and Kendall, J. M. (2019). Geophysical Monitoring of Moisture-Induced Landslides: A Review, *Reviews of Geophysics*, Vol. 57, No. 1, 106–145. doi:10.1029/2018RG000603.
4. Perrone, A., Lapenna, V., and Piscitelli, S. (2014). Electrical Resistivity Tomography Technique for Landslide Investigation: A Review, *Earth-Science Reviews*, Vol. 135, 65–82. doi:10.1016/j.earscirev.2014.04.002.
5. Tsai, W.-N., Chen, C.-C., Chiang, C.-W., Chen, P.-Y., Kuo, C.-Y., Wang, K.-L., Lin, M.-L., and Chen, R.-F. (2021). Electrical Resistivity Tomography (ERT) Monitoring for Landslides: Case Study in the Lantai Area, Yilan Taiping Mountain, Northeast Taiwan, *Frontiers in Earth Science*, Vol. 9, 737271. doi:10.3389/feart.2021.737271.
6. Wicki, A., and Hauck, C. (2022). Monitoring Critically Saturated Conditions for Shallow Landslide Occurrence Using Electrical Resistivity Tomography, *Vadose Zone Journal*, Vol. 21, No. 4, e20204. doi:10.1002/vzj2.20204.
7. Vivaldi, V., Torrese, P., Bordoni, M., Viglietti, F., and Meisina, C. (2024). ERT-Based Experimental Integrated Approach for Soil Hydrological Characterization in Rainfall-Induced Shallow Landslides Prone Areas, *Bulletin of Engineering Geology and the Environment*, Vol. 83, No. 5, 167. doi:10.1007/s10064-024-03627-8.
8. Pazzi, V., Morelli, S., and Fanti, R. (2019). A Review of the Advantages and Limitations of Geophysical Investigations in Landslide Studies, *International Journal of Geophysics*, Vol. 2019, 1–27. doi:10.1155/2019/2983087.
9. Himi, M., Anton, M., Sendrós, A., Abancó, C., Ercoli, M., Lovera, R., Deidda, G. P., Urruela, A., Rivero, L., and Casas, A. (2022). Application of Resistivity and Seismic Refraction Tomography for Landslide Stability Assessment in Vallcebre, Spanish Pyrenees, *Remote Sensing*, Vol. 14, No. 24, 6333. doi:10.3390/rs14246333.
10. Olabode, O. P., Lim, H. S., and Ramli, M. H. (2022). Geophysical and Geotechnical Evaluation of Landslide Slip Surface in a Residual Soil for Monitoring of Slope Instability, *Earth and Space Science*, Vol. 9, No. 12, e2022EA002248. doi:10.1029/2022EA002248.
11. Huayllazo, Y., Infa, R., Soto, J., Lazarte, K., Huanca, J., Alvarez, Y., and Teixidó, T. (2023). Using Electrical Resistivity Tomography Method to Determine the Inner 3D Geometry and the Main Runoff Directions of the Large Active Landslide of Pie de Cuesta in the Vítor Valley (Peru), *Geosciences*, Vol. 13, No. 11, 342. doi:10.3390/geosciences13110342.
12. Ali, B., Nanda, M., Zainal, M., Yanis, M., Surbakti, M. S., Idris, N., and Ismail, N. (2024). Application of ERT, IP and VLF-EM Methods to Investigate Landslide-Prone Structures at Archaeological Sites in Lamreh, Aceh Besar, Indonesia, *Trends in Sciences*, Vol. 21, No. 3, 7221. doi:10.48048/tis.2024.7221.
13. Zainal, M., Munir, B., and Marwan. (2021). The Electrical Resistivity Tomography Technique for Landslide Characterization in Blangkejeren Aceh, *Journal of Physics: Conference Series*, Vol. 1825, No. 1, 012022. doi:10.1088/1742-6596/1825/1/012022.
14. Zainal, M., Munir, B., Marwan, M., Yanis, M., and Muhni, A. (2021). Characterization of Landslide Geometry Using Seismic Refraction Tomography in the GayoLues, Indonesia, *Journal of Physics and Its Applications*, Vol. 3, No. 2, 148–154. doi:10.14710/jpa.v3i2.10601.
15. Regency, B.-S. of G. L. (2020). *Gayo Lues Regency in Figures 2020*Blangkejeren, BPS-Statistics of Gayo Lues Regency.
16. Cameron, N. R., Bennett, J. D., Djunuddin, A., Ghazali, S. A., Harahap, H., Jeffery, D. H., Kartawa, W., Keats, W., Ngabito, H., Rocks, N. M. S., and Thompson, S. J. (1983). Geologic Map of the Takengon Quadrangle, Sumatra, Geological Research and Development Center.
17. Sieh, K., and Natawidjaja, D. (2000). Neotectonics of the Sumatran Fault, Indonesia, *Journal of Geophysical Research: Solid Earth*, Vol. 105, No. B12, 28295–28326. doi:10.1029/2000JB900120.
18. Burton, P. W., and Hall, T. R. (2014). Segmentation of the Sumatran Fault, *Geophysical Research Letters*, Vol. 41, No. 12, 4149–4158. doi:10.1002/2014GL060242.
19. Dahlin, T., and Zhou, B. (2004). A Numerical Comparison of 2D Resistivity Imaging with 10 Electrode Arrays, *Geophysical Prospecting*, Vol. 52, No. 5, 379–398. doi:10.1111/j.1365-2478.2004.00423.x.
20. Oldenburg, D. W., and Li, Y. (1999). Estimating Depth of Investigation in DC Resistivity and IP Surveys, *Geophysics*, Vol. 64, No. 2, 403–416. doi:10.1190/1.1444545.
21. Sun, M., Liu, J., Ou, J., Liu, R., and Zhu, L. (2024). Electrical Resistivity Tomography (ERT) Investigation for Landslides: Case Study in the Hunan Province, China, *Applied Sciences*, Vol. 14, No. 7, 3007. doi:10.3390/app14073007.
22. Chibani, A., Hebbache, K., Mellas, M., and Mabrouki, A. (2023). 2D Electrical Resistivity Tomography (ERT) Investigation of a Landslide: A Case Study from Ali Mendjeli, Constantine, North-East of Algeria, *NRIAG Journal of Astronomy and Geophysics*, Vol. 12, No. 1, 45–57. doi:10.1080/20909977.2022.2163787.
23. Santosa, I., Sulaksana, N., Yuningsih, E. T., and Zakaria, Z. (2024). The Sliding Surface Determination of A Deep-Seated Landslide on Cisumdawu Highway, West Java, Based on The Electrical Resistivity Tomography, *Indonesian Journal on Geoscience*, Vol. 11, No. 2, 189–199. doi:10.17014/ijog.11.2.189-199.
24. Bordoni, M., Vivaldi, V., Lucchelli, L., Ciabatta, L., Brocca, L., Galve, J. P., and Meisina, C. (2021). Development of a Data-Driven Model for Spatial and Temporal Shallow Landslide Probability of Occurrence at Catchment Scale, *Landslides*, Vol. 18, No. 4, 1209–1229. doi:10.1007/s10346-020-01592-3.
25. Fusco, F., Bordoni, M., Tufano, R., Vivaldi, V., Meisina, C., Valentino, R., Bittelli, M., and De Vita, P. (2022). Hydrological Regimes in Different Slope Environments and Implications on Rainfall Thresholds Triggering Shallow Landslides, *Natural Hazards*, Vol. 114, No. 1, 907–939. doi:10.1007/s11069-022-05417-5.